Journal of Nanofluids
Vol. 12, pp. 2310–2323, 2023
(www.aspbs.com/jon)

ARTICLE

Effects of Pressure Gradient on Fluid Flow and Energy Distribution in a Bending Square Channel

Rabindra Nath Mondal[1], Sreedham Chandra Adhikari[1], Ratan Kumar Chanda[1], Mohammad Ghalambaz[2,3], and Mohammad S. Islam[4,*]

[1]*Department of Mathematics, Jagannath University, Dhaka, 1100, Bangladesh*
[2]*Metamaterials for Mechanical, Biomechanical and Multiphysical Applications Research Group, Ton Duc Thang University, Ho Chi Minh City, Vietnam*
[3]*Faculty of Applied Sciences, Ton Duc Thang University, Ho Chi Minh City, Vietnam*
[4]*School of Mechanical and Mechatronic Engineering, Faculty of Engineering and Information Technology, University of Technology Sydney, Ultimo, NSW, 2007, Australia*

A precise knowledge on fluid flow and energy distribution in a bending channel is important for the thermal management of various engineering problems. The literature currently lacks a comprehensive understanding on how fluid characteristics and heat transfer in a bending channel are affected by pressure gradients, as well as when and how fluids transit into a turbulent state under continuous pressure gradient. The present study aims to explore the bifurcation structure of the steady solutions, linear stability and velocity distribution of the solutions and the transitional behavior from stead-state to other flow states (i.e., periodic or chaotic) for an extensive domain of the Dean number $0 < Dn \leq 5000$. The geometry of the problem is that the outer and bottom walls are heated while the inner and top are at room temperature. A proper grid analysis and validation are performed as well. The study successfully analyzed four branches of steady solutions where stability exists only in the first branch up to $Dn = 2593.3709$ and 2- to 7-vortex solutions are observed in the secondary flow. The flow transitions in the unsteady solutions are analyzed exquisitely by performing time-advancement of the solutions followed by inquisition of the phase space of time-dependent solutions. Results show that, if $Dn > 2593.3709$, the steady-state flow becomes periodic followed by a chaotic solution and 2- to 5-vortex solutions are observed for the unsteady flow. It is noticed that, if $Dn > 0$, the value of the Nusselt number (Nu) was initially higher on the cooling wall compared to the heated wall and at $Dn = 102.67$, Nu is found to be equal on both sidewalls and then it started increasing rapidly on the heated walls. The present study figured out how centrifugal force impacts fluid flow for larger pressure gradient, which assists fluid mixing and consequently enhances heat transfer in the fluid.

KEYWORDS: Bending Duct, Branching Structure, Secondary Flow, Energy Distribution, Pressure Gradient.

1. INTRODUCTION

Over the last few decades, the exploration of fluid flow (FF) and heat transfer (HT) is going on due to grandiose applications from industrial fields to medical services, and researchers are engrossed to research various flow phenomena through a straight pipe to bending pipe (BP). Researchers were stupefied when they observed the formation of secondary flow (SF) in the cross-section (CS) of a BP, which is taken place under the response of centrifugal force (CF) due to duct curvature, and still, these phenomena attract the forthcoming researchers to work on it. Many practical applications are based on BP, for instance, heat exchangers, solar energy, ventilators, air conditioning systems, chemical reactors, combustion engines, etc. Curved duct (CD), indeed, is one of the most impressive geometrical designs where many scholars found their interest in researching it and improving it to obtain better outcomes day by day. Based on the shape of BP, several articles/papers are accomplished by the scholars, referenced by Mondal et al.,[1,2] Goharzadeh and Rodgers[3] for rectangular curved duct, Hille et al.,[4] and Mondal et al.[5] for square duct, Chatterjee et al.[6] for cylindrical system, Song et al.[7] for elliptical duct, Parvin et al.[8] and Toghraie et al.[9] for annulus of circular cross-section and so on.

Numerous impressive features have arisen from the duct curvature while investigating the flow in a CD–Bifurcation structure (BS) is one of them. Understanding

*Author to whom correspondence should be addressed.
Emails: mohammadsaidul.islam@uts.edu.au, rnmondal71@yahoo.com
Received: 22 March 2023
Accepted: 18 May 2023

the bifurcation structure of a system can provide important insights into its behavior and help to predict its response to changes in its controlling parameters. This knowledge can be useful in a wide variety of applications, from predicting the onset of turbulence in fluid flows to designing control systems for industrial processes. The dramatic bifurcation structure is a potential scheme to figure out the flow structure in a steady solution (SS). It is known that the general flow pattern in straight duct changes into a complex structure in bend duct (BD) and this incident occurs due to the Centrifugal force (CF), which produces secondary flow (SF) in the cross-section of the duct. Dean[10, 11] first introduced us to a couple of converse rotating vortices arising in the cross-section of a BD, and under particular flow conditions, these pair of vortices turn into a four-vortex solution. The branching structure in steady solution is explored by Mondal et al.[12] using a CRD for a fixed $Gr = 1000$ over the range $0 < Dn \leq 1000$ for various curvature ratios, $0 < \delta \leq 0.5$, where they obtained five asymmetric SS branches and these are composed of a single-vortex to eight-vortex solution for several Dn. Through the current works, Hasan et al.[13–15] observed the combined consequences of Coriolis, buoyancy, centrifugal force, the interconnection of BS, and time advancement flow for both revolving and non-revolving square ducts. However, the authors have some limitations to concentrate on the impact of parameters while investigating flow transition and also to inspect the AF and SF over the grid points. While, in many previous works, less attention is made to strong CF, and therefore, due to extensive demand in engineering sectors, this study will enrich the buoyancy-influenced centrifugal force.

One of the major features of the time-dependent flow is its transient i.e., the time-dependent flow, which attracts considerable attention in the scientific society after Yanase and Nishiyama[16] who first introduced us to the unsteady flow (UF) in a CRD by exploring the non-linear behavior of the UF. Mondal et al.[17] conducted a numerical analysis on UF for small aspect ratio (0.5) and moderate curvature (0.1) in a non-cyclic CRD with an external heated wall. The 2-vortex steady-state flow turned into periodic flow with 3 and 4-vortex solution thereafter, and the only chaotic solution consisting of 2-vortex was obtained for $Dn = 10000$ when $Gr = 2000$. Chamkha[18] analyzed the time history of heat transfer coefficients varying the temperature inverse stokes number where it was stated that increasing the coefficients values increase the energy transfer between the fluid and the particle-phases. Ray et al.[19] explored the hydrodynamic instability of 2D viscous incompressible fluid through a revolving CRD with the bottom heating using a numerical approach in the positive direction only. Here, two- to ten-vortex SF was found in the obtained three asymmetric SS branches, and in the unsteady solutions, flow transitions were obtained justifying by PSD. They predicted that the flow will first transform from chaotic to regular fluctuation, and then arrive at a steady-state solution.

To understand the convection of HT from the walls to the fluid through bend channel, scientists and researchers are enticed much because of plentiful applications. HT in channels has various applications in the metallurgy industry, chemical industry, steam generation, aerospace engineering, nuclear engineering. The plausibility of heat convection may be affected by the channel curvature and corresponding flow parameters. Islam et al.[20] research utilized both positive and negative rotating CRD with two distinct Dn's. Careful examination of the effects of Dn-Tr flow in the unstable solutions and CHT revealed that the HC was boosted more by the 8-vortex chaotic flow than by the 2-vortex steady-state. Two- to twelve-vortex SF in four steady branches is obtained by Chanda et al.[21–24] through the inquisition of the impact of heat-flux on fluid flow and energy ordination in a CRD. Chatterjee et al.[6] and Manna et al.[25] investigated the influence of heater-cooler position in thermal management, where they stated that the location of the heated source and cold sink on the enclosure geometry can have a considerable impact on the thermo-fluid phenomenon. Most of the studies mentioned above are explored using large or small curvature; a moderate curvature is considered less, but the current study will reduce this gap due to grandiose engineering applications.

In this paper, the mysterious structure of flow and energy ordination in a BSD is investigated by looking for steady solutions, examining linear stability, and executing non-linear activities of the flow by time-evolution computation with phase-space analysis of the flow development. The study also explains and demonstrates a novel computational approach for detecting the onset of hydrodynamic instability with heat-flux effects in BC, which is evidenced by the creation of Dean vortices.

2. FORMATION OF GOVERNING EQUATIONS

To govern the mathematical formulae of the present study, a bent channel of square cross-section (height = width = $2d$) is considered, which has outer-bottom walls heated and the inner-ceiling cooled, and the viscous, laminar 2D fluid (water) is conjectured which passes away through the center-line of the channel (see Adhikari et al.,[26] Hasan et al.[27]) The schematic diagram with pertinent notations is described in Figure 1, in which C is the kernel of the cross-section, O is the center of the duct, and L is the radius of the curvature. A cylindrical coordinate (r, θ, z) is supposed, where, r = radius vector, θ = azimuthal angle, and z = coordinate along with the cylinder, to formulate the mathematical terms as follows:

Continuity equation:

$$\frac{\partial q_r}{\partial r} + \frac{1}{r} q_r + \frac{1}{r'} \frac{\partial q_\theta}{\partial \theta} + \frac{\partial q_z}{\partial z} = 0 \qquad (1)$$

ARTICLE

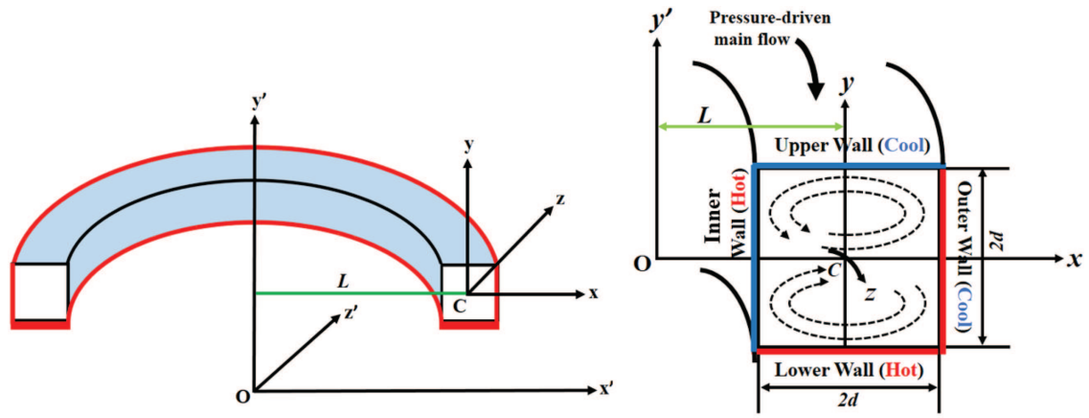

Fig. 1. (a) Coordinate system (b) cross-sectional view.

Navier-Stokes equations:

$$\frac{\partial q_r}{\partial t}+(\nu\cdot\nabla)q_r-\frac{q_\theta^2}{r}=-\frac{1}{\rho}\frac{\partial P}{\partial r}+\nu\left(\tilde{\Delta}q_r-\frac{q_r}{r^2}-\frac{2}{r^2}\frac{\partial q_\theta}{\partial\theta}\right) \tag{2}$$

$$\frac{\partial q_\theta}{\partial t}+(\nu\cdot\nabla)q_\theta+\frac{q_r q_\theta}{r}=-\frac{1}{\rho r}\frac{\partial P}{\partial\theta}+\nu\left(\tilde{\Delta}q_\theta-\frac{q_\theta}{r^2}+\frac{2}{r^2}\frac{\partial q_r}{\partial\theta}\right) \tag{3}$$

$$\frac{\partial q_z}{\partial t}+(\nu\cdot\nabla)q_z=-\frac{1}{\rho}\frac{\partial P}{\partial z}+\nu\tilde{\Delta}q_r+\beta g\Im \tag{4}$$

Energy equation:

$$\frac{\partial\Im}{\partial t}+(\nu\cdot\nabla)\Im=\kappa\tilde{\Delta}\Im \tag{5}$$

$$\text{where,}\quad (\nu\cdot\nabla)=q_r\frac{\partial}{\partial r}+\frac{q_\theta}{r}\frac{\partial}{\partial\theta}+q_z\frac{\partial}{\partial z};$$

$$\tilde{\Delta}=\frac{\partial^2}{\partial r^2}+\frac{1}{r}\frac{\partial}{\partial r}+\frac{1}{r^2}\frac{\partial^2}{\partial\theta^2}+\frac{\partial^2}{\partial z^2}$$

Herein, q_r, q_θ and q_z are the velocity components in the r, θ, and z directions continuously, and the notations ρ, γ, β, g and κ are the density, kinetic viscosity, momentum factor, gravitational acceleration, and coefficient of thermal conductivity, respectively. The coordinate (r, θ, z) is transmuted to Cartesian form using the following transformations:

$$L=r+dx,\quad L\theta=-dz,\quad z=hy,\quad q_r=q_x=U_0u,$$

$$q_z=q_y=U_0v,\quad q_\theta=-q_z=U_0w,\quad P^*=\rho{U_0}^2P,$$

$$\delta=\frac{d}{L},\quad G=-\frac{\partial P^*}{\partial z}\frac{d}{\rho{U_0}^2}$$

Now, Stream function (ζ) introduces the continuity equation in the x- and y- directions as

$$u=\frac{1}{\ell}\frac{\partial\zeta}{\partial y}\quad\text{and}\quad v=-\frac{1}{\ell}\frac{\partial\zeta}{\partial x};\quad\text{where, }\ell=1+\delta x.$$

Following the previous works by Yanase and Nishiyama[16] and Winters,[28] the derived non-dimensional equations for α, ζ and $\Im$ are as follows.

$$\ell\frac{\partial\alpha}{\partial t}=Dn+\ell\tilde{\Delta}_2\alpha-\frac{\partial(\alpha,\zeta)}{\partial(x,y)}-\eta\delta\alpha-\eta\frac{\partial\zeta}{\partial y}\alpha+\delta\frac{\partial\alpha}{\partial x} \tag{6}$$

$$\left(\tilde{\Delta}_2-\eta\frac{\partial}{\partial x}\right)\frac{\partial\zeta}{\partial t}$$

$$=-\frac{1}{\ell}\frac{\partial(\tilde{\Delta}_2\zeta,\zeta)}{\partial(x,y)}+\frac{\eta}{\ell}\left[\frac{\partial\zeta}{\partial y}\left(2\tilde{\Delta}_2\zeta-3\eta\frac{\partial\zeta}{\partial x}+\frac{\partial^2\zeta}{\partial x^2}\right)\right.$$

$$\left.\times\frac{\partial\zeta}{\partial x}\frac{\partial^2\zeta}{\partial x\partial y}\right]+\frac{\eta}{\ell}\times\left[3\delta\frac{\partial^2\zeta}{\partial x^2}-3\eta\delta\frac{\partial\zeta}{\partial x}\right]$$

$$-2\eta\frac{\partial}{\partial x}\tilde{\Delta}_2\zeta+\alpha\frac{\partial\alpha}{\partial y}+\tilde{\Delta}_2^2\zeta-\ell Gr\frac{\partial\Im}{\partial x} \tag{7}$$

$$\frac{\partial\Im}{\partial t}=\frac{1}{Pr}\left(\tilde{\Delta}_2\Im+\frac{\delta}{\ell}\frac{\partial\Im}{\partial x}\right)-\frac{1}{\ell}\frac{\partial(\Im,\zeta)}{\partial(x,y)} \tag{8}$$

$$\text{Where,}\quad \eta=\frac{\delta}{\ell};\quad \ell=1+\delta x,\quad \tilde{\Delta}_2=\frac{\partial^2}{\partial x^2}+\frac{\partial^2}{\partial y^2},$$

$$\frac{\partial(\Im,\zeta)}{\partial(x,y)}=\frac{\partial\Im}{\partial x}\frac{\partial\zeta}{\partial y}-\frac{\partial\zeta}{\partial x}\frac{\partial\Im}{\partial y}$$

The dimensionless parameters Dn, Gr, Pr, and δ used in the Eqs. (6)–(8), are defined in Chanda et al.[22] These dimensionless parameters are the cause of fluid acceleration and energy distribution; the Dean number (Dn)—a pressure gradient parameter that accelerates fluid flow in the axial direction; the Grashof number (Gr)—a buoyancy force parameter which creates temperature differences between the applied hot and cold walls; the Prandtl number— a characteristic fluid defining parameter to predict the onset of turbulent flow in a fluid, as well as to model the heat transfer behavior of a fluid; the curvature (δ)–a ratio of inner radius to outer radius of the duct which

is specially used to create centrifugal force. The other non-dimensional terms we have used are α, ζ and $\Im$ that are respectively axial flow defining parameter, stream function and energy distribution.

Boundary conditions for α and ζ are taken as

$$\left.\begin{aligned} \alpha = \zeta = \frac{\partial \zeta}{\partial x} = 0 \quad \text{at} \quad x = \pm 1, \quad y = y \\ \alpha = \zeta = \frac{\partial \zeta}{\partial x} = 0 \quad \text{at} \quad x = x, \quad y = \pm 1 \end{aligned}\right\} \tag{9a}$$

and the thermal boundary conditions for the geometrical body (SD) are set up as

$$\left.\begin{aligned} \Im = y \quad \text{at} \quad x = \pm 1, \quad y = y \\ \Im = x \quad \text{at} \quad x = x, \quad y = \pm 1 \end{aligned}\right\} \tag{9b}$$

3. NUMERICAL ANALYSIS

3.1. Method of Numerical Procedure

The spectral element method is used while executing the equations from (6) to (8). To get the required solutions, the n-th order Chebyshev polynomials ($\Omega_n(x) = \cos\left(n\cos^{-1}(x)\right)$) is taken to extend the flow defining parameters. The expanding functions $\varphi_n(x)$ and $\psi_n(x)$ are enunciated as

$$\left.\begin{aligned} \varphi_n(x) = (1-x^2)\Omega_n(x) \\ \psi_n(x) = (1-x^2)^2\Omega_n(x) \end{aligned}\right\} \tag{10}$$

The axial velocity $\alpha(x, y, t)$, secondary flow $\zeta(x, y, t)$, and temperature distribution $\Im(x, y, t)$ are extended in terms of $\varphi_n(x)$ and $\psi_n(x)$ as

$$\left.\begin{aligned} \alpha(x,y,t) = \sum_{m=0}^{M}\sum_{n=0}^{N} \alpha_{mn}(t)\ \varphi_m(x)\ \varphi_n(y) \\ \zeta(x,y,t) = \sum_{m=0}^{M}\sum_{n=0}^{N} \zeta_{mn}(t)\ \psi_m(x)\ \psi_n(y) \\ \Im(x,y,t) = \sum_{m=0}^{M}\sum_{n=0}^{N} \Im_{mn}(t)\ \varphi_m(x)\ \varphi_n(y) + x - y \end{aligned}\right\} \tag{11}$$

Here, the collocation points (x_i, y_j) are chosen to be

$$\begin{aligned} x_i &= \cos\left[\pi\left(1 - \frac{i}{M+2}\right)\right], \\ y_j &= \cos\left[\pi\left(1 - \frac{j}{N+2}\right)\right] \end{aligned} \tag{12}$$

where, $i = 1, 2, 3, \ldots, M+1$, $j = 1, 2, 3, \ldots, N+1$ and $M = N = 20$.

The expanded coefficients of functions are α_{mn}, ζ_{mn} and $\Im_{mn}$. Newton-Raphson method (arc-length method) as well as the collocation method is adopted to find a steady solution, and Crank-Nicholson, Adam-Bashforth, and the function expansions (11) are enforced to obtain unsteady solutions. The details of the above-mentioned methods are conveyed by Mondal et al.[29] and Gottlieb and Orszag.[30]

3.2. Hydrodynamic Resistance Coefficient

The resistance coefficient (λ) is defined as (Hasan et al.[31]):

$$\frac{\tilde{p}_1^* - \tilde{p}_2^*}{\Delta_z} = \frac{\lambda}{d_h}\frac{1}{2}\rho\langle\tilde{\alpha}\rangle^2 \tag{13}$$

where d_h presents the hydraulic diameter. The main axial velocity $\langle\tilde{\alpha}\rangle$ is obtained by

$$\langle\tilde{\alpha}\rangle = \frac{v}{4\sqrt{2\delta d}}\int_{-1}^{1} dx \int_{-1}^{1} \alpha\,(x, y, t)\,dy \tag{14}$$

The resistance coefficient (λ) and the mean axial velocity $\langle\tilde{\alpha}\rangle$ are related as

$$\lambda = \frac{4\sqrt{2\delta}Dn}{\langle\tilde{\alpha}\rangle^2} \tag{15}$$

3.3. The Nusselt Number (*Nu*)

To acquire the Nusselt number (*Nu*) as described by Hasan et al.[32] from the steady solution, the following formula is used.

$$Nu = -\frac{d^*}{\Delta\Im}\left\langle \left.\frac{\partial\Im}{\partial x}\right|_{x=0} \right\rangle \tag{16}$$

Here, the dimensionless quantities are assigned by the asterisk symbol ($*$) and the sign $\langle\rangle$ represents the average heat transmission from walls to fluid, x is the distance of the walls, and $\Delta\Im$ is the temperature difference applied between the cooled and heated sidewalls. Again, for unsteady solutions, *Nu* is obtained by the formula

$$\begin{aligned} Nu_{\tau_c} &= \frac{1}{2}\int_{-1}^{1} \left\langle\left\langle \left.\frac{\partial\Im}{\partial x}\right|_{x=-1} \right\rangle\right\rangle dy, \\ Nu_{\tau_h} &= \frac{1}{2}\int_{-1}^{1} \left\langle\left\langle \left.\frac{\partial\Im}{\partial x}\right|_{x=1} \right\rangle\right\rangle dy \end{aligned} \tag{17}$$

Where the symbol $\langle\langle\rangle\rangle$ assigns an average over the time interval. For periodic vacillation, τ is ordained as one period, but for a chaotic stream, τ is picked to be an appropriate time interval.

3.4. Grid Efficacy

The algorithm used in the present study for the governing equations will be validated by the grid efficacy since it is an effective method to justify how much error produces when calculating the numerical approximation. Hasan et al.[14] executed the grid efficiency for $Tr = 1000$ and $Tr = -1000$ in a rotating CSD through the representation of relative percentage error and finally applied 22×22 grid size in their study. Wang et al.[33] visualized the variation of BS with the variation of grid points. In our study, the resistance coefficient (λ) and the axial velocity (ω) are used to check the grid accuracy using the values of $Dn = 1000$, $Gr = 1000$, $Ar = 1.0$, $Pr = 7.0$, $\delta = 0.1$ for various grid sizes such as 14×14, 16×16, etc. The percentage error for both λ and ω using the grid size and the

ARTICLE

Table I. Values of λ, $\varepsilon_p(\lambda)$, $\alpha(0,0)$, and $\varepsilon_p(\alpha)$ for various M and N $(=M)$ at $Dn = 1000$, $Gr = 1000$, $Pr = 7.0$, and $\delta = 0.1$.

M	N	λ	Relative error $\varepsilon_p(\lambda)$	$\alpha(0,0)$	Relative error $\varepsilon_p(\alpha)$
14	14	0.2424961774	–	359.2288895949	–
16	16	0.2424391761	0.0235115879%	359.4094473751	0.0502373495%
18	18	0.2424564274	0.0071152166%	359.7381430008	0.0913708018%
20	**20**	**0.2424612487**	**0.0019884827%**	**359.8802357404**	**0.0394833406%**
22	22	0.2424546468	0.0027229422%	360.0006173145	0.0334392688%
24	24	0.2424575521	0.0011982716%	360.0097467922	0.0275283385%

percentage errors are represented in Table I and plotted in Figures 2(a) and (b), respectively. The percentage errors are obtained using the formula,

$$\varepsilon_p = \left| \frac{\text{current value} - \text{previous value}}{\text{current value}} \right| \times 100\%$$

It is seen from the Table I as well as from Figures 2(a) and (b) that $\varepsilon_p(\lambda)$ changes 0.0235115879% and $\varepsilon_p(\omega)$ changes 0.0502373495% from $M = 14$ to $M = 16$. Then $\varepsilon_p(\lambda)$ reduces but $\varepsilon_p(\omega)$ increases with the increment of M from 16 to 18. The changes of $\varepsilon_p(\lambda)$ and $\varepsilon_p(\omega)$ from $M = 18$ to $M = 20$ are 0.0019884827% and 0.0394833406% correspondingly. A closer look at Table I shows that the percentage errors obtained for $M = 22$ and $M = 24$ are comparatively negligible than $M = 20$. Therefore, $M = 20$, $N = 20$ grid sizes (boldfaces in Table I) are applied to the present numerical calculations which assures substantial accuracy.

3.5. Experimental versus Numerical Outcomes

In order to confirm the accuracy and authenticity of secondary flow structures, the numerical results of SF structures are compared with the findings of the experiments. The experimental studies by Wang and Yang[34] for the CSD reported the SF of the current paper. The investigation is described here for not just the non-rotating situation but also the rotational case. Figure 3 on the left displays the SF patterns for the experimental results, while Figure 3 on the right shows the numerical results.

Wang and Yang[34] conducted the experiments that resulted in Figure 3. Their study was the first to look at

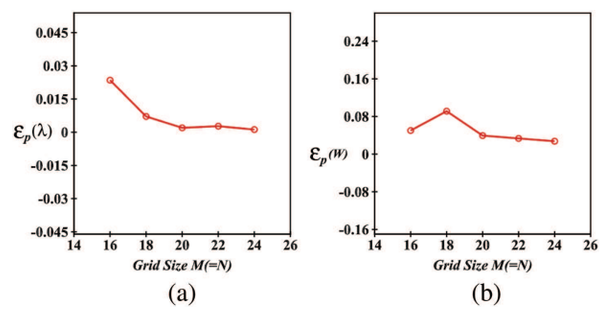

Fig. 2. Relative percentage errors with respect to grid sizes, (a) $\varepsilon_p(\lambda)$ and (b) $\varepsilon_p(\alpha)$.

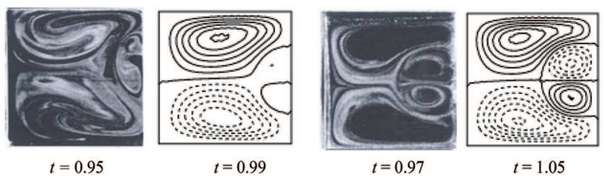

Fig. 3. Comparison between numerical and experimental results. Left: Experimental view by Wang and Yang,[34] right: numerical view by the authors. Reproduced with permission from L. Wang and T. Yang, *Physica D: Nonlinear Phenomena* 200, 296 (**2005**). Copywright © 2004 Elsevier.

how flow patterns changed over time. In their study, the experimental duct had a curvature ratio of 0.4, and the flows were detected in 270° inlet. For validation purposes, the Prandtl number and curvature ($Pr = 7.0$ and $\delta = 0.1$) have been converted into $Pr = 0.7$ (air) and $\delta = 0.04$, respectively. The computation of the time evolution of the unstable solutions is investigated after changing the parameter, revealing the flow patterns as illustrated on the right side of Figure 3. It can be shown that the flow structures in the computational and experimental studies are identical.

4. RESULTS AND DISCUSSION

4.1. Branching Structure of Steady Solutions (SS) with Linear Stability

Following the pertinent parametric values conferred in Table II, an explicit numerical investigation is accomplished through the discussion of SS branching structure with linear stability analysis.

Over the parametric ranges in Table II, we obtained four asymmetric SS branches termed the 1st, 2nd, 3rd, and 4th branches, respectively. A bifurcation diagram is sketched in Figure 4(a), showing the four branches of SS synchronically in the λ-determinative quantity (resistance coefficient) of the flow state versus the Dn plane. Newton-Raphson iteration method with path continuation approach and multifarious initial presumptions are used to find out the SS branches, which are distinguished by the counting of the secondary vortices. In Figure 4(a), the red solid line illustrates the 1st branch, where the green dotted line, blue dash-dot line, and the orange dash-dot-dot line represent the 2nd, 3rd, and 4th branch successively. Due to the dense branching structure in the higher region of Dn, an enlargement of the intertwined area from $Dn = 3700$ to 4850 is shown in Figure 4(b). This suggests that each

Table II. Relative variables and values considered in the current exploration.

Variables	Considered value/ranges	Comments
Aspect ratio (Ar)	1.0	Square duct
Curvature (δ)	$\delta = 0.1$	Moderate curvature
Grashof number (Gr)	1000	Buoyancy parameter
Prandtl number (Pr)	7.0	Water
Dean number (Dn)	$0 < Dn \leq 5000$	Pressure-gradient parameter

branch represents a distinct flow state characterized by its own set of secondary vortices.

The first SS branch exists throughout the whole working domain of Dn ($0 < Dn \leq 5000$), comprising several turning points, which is depicted in Figure 5(a). The branch starts with increasing Dn and decreasing λ from $Dn = 0$ at $\lambda \approx \infty$, but whenever any turning point arises in its way, the direction of both Dn and λ changes. The obtained turning points in the 1st branch are $Dn = 4823.2852$ ($\lambda = 0.1107$), $Dn = 3647.0031$ ($\lambda = 0.1228$), $Dn = 4976.1464$ ($\lambda = 0.1084$), $Dn = 3862.0483$ ($\lambda = 0.1234$), $Dn = 4157.0848$ ($\lambda = 0.1194$), $Dn = 2529.5096$ ($\lambda = 0.1487$), and finally ended at $Dn = 5000$ ($\lambda = 0.1094$). A small portion of the perplexing branching structure for larger Dn ($3650 \leq Dn \leq 4180$) is expanded and clearly shows the complexity of the branch. The second SS branch is drawn exclusively in Figure 5(b), which is existed in the zone of Dn, $680.6206 \leq Dn \leq 5000$ with various smooth, sharp and entangled turning points. It begins from $Dn = 5000$ at $\lambda = 0.1094$, then prolongs with numerous turnings consecutively as $Dn = 680.6206$ ($\lambda = 0.3041$), $Dn = 1014.0421$ ($\lambda = 0.2636$), $Dn = 1000.8998$ ($\lambda = 0.2657$), $Dn = 1878.9926$ ($\lambda = 0.1968$), $Dn = 1610.2117$ ($\lambda = 0.2116$), $Dn = 1699.1521$ ($\lambda = 0.2055$), $Dn = 1447.2985$ ($\lambda = 0.2229$), $Dn = 2755.6673$ ($\lambda = 0.1611$), $Dn = 2747.2804$ ($\lambda = 0.1612$) and then converges to $Dn = 5000$. The 3rd steady branch is sketched in Figure 6(a), which covers the Dn, $2107.7794 \leq Dn \leq 5000$ with an enlarged view of a small section of Dn, $3738 \leq Dn \leq 4152$, which shows the intricacy of the branch. Similar to 2nd branch, it also extends from $Dn = 5000$ at $\lambda = 0.1227$, then prolongs in its way facing several inclination points such as $Dn = 4944.9177$ ($\lambda = 0.1233$), $Dn = 4965.9556$ ($\lambda = 0.1224$), $Dn = 2107.7794$ ($\lambda = 0.1861$), $Dn = 4095.6265$ ($\lambda = 0.1395$), $Dn = 3858.9004$ ($\lambda = 0.1417$), $Dn = 3965.4243$ ($\lambda = 0.1406$), $Dn = 3758.9503$ ($\lambda = 0.1414$), $Dn = 4808.6157$ ($\lambda = 0.1264$), $Dn = 4266.8985$ ($\lambda = 0.1337$), $Dn = 5000$ ($\lambda = 0.1277$). The 4th branch is the smallest branch covering a small region of Dn ($2794.5493 \leq Dn \leq 5000$) with a smooth single inclination point ($Dn = 2794.5493$ at $\lambda = 0.1543$), which is displayed in Figure 6(b).

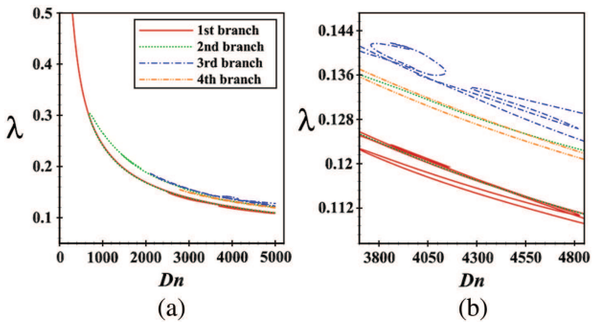

Fig. 4. (a) Branching structure of SS (b) Enlargement of (a) for larger Dn.

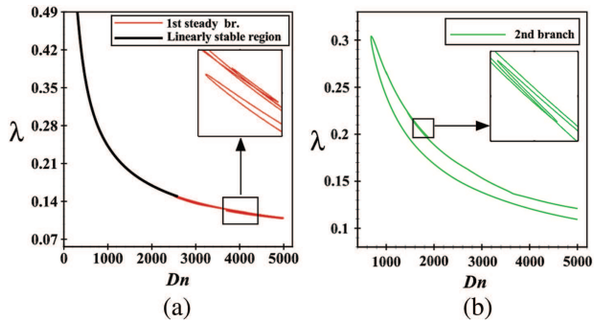

Fig. 5. Composition of (a) 1st SS branch with the linearly stable region, (b) 2nd SS branch.

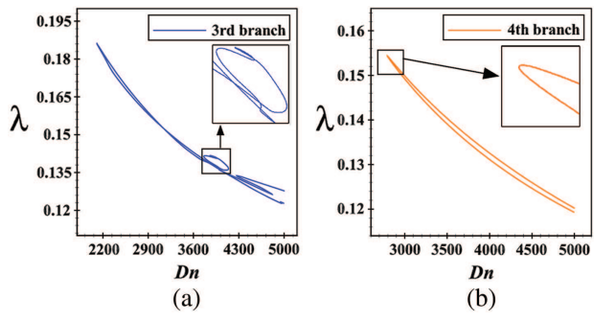

Fig. 6. (a) Composition of (a) 3rd SS branch, (b) 4th SS branch.

To discuss the linearity of the SS branches, i.e., to find out the stable and unstable regions, a two-dimensional perturbations formula is used. Hasan et al.[35] and Mondal et al.[29] discussed the stability of the steady branches and recapitulated the perturbation technique. The exploration of linear stability through the SS branches in Table III provides us that only 1st branch is linearly stable on $0 < Dn \leq 2593.3709$ (boldface in Table III). This indicates that small perturbations applied to this branch will decay over time, maintaining the steady-state nature of the flow. However, for the range of $2593.3710 \leq Dn \leq 5000$, the branch becomes linearly unstable. In this region, small perturbations can lead to significant disturbances and alter the flow behavior. The linearly stable region is plotted in Figure 5(a) with a bold black solid line. Also, the stability region with respect to Dn in a pie chart is depicted in Figure 7. It is seen that 51.87% of the total

ARTICLE

Table III. Linear stability of 1st steady branch for $\delta = 0.1$.

Dn	λ	σ_r	σ_i	Characteristics
10	**9.25212524444**	**−1.1711**	**0**	Linearly stable
1000	**0.242571453389**	**−1.7881**	**0**	Linearly stable
2592.8851	**0.148877594763**	$\mathbf{-5.8061 \times 10^{-03}}$	$\mathbf{9.9242 \times 10^{01}}$	Linearly stable
2593.3708	**0.148864074227**	$\mathbf{-1.4306 \times 10^{-06}}$	$\mathbf{9.9271 \times 10^{01}}$	Linearly stable
2593.3709	**0.148864071444**	$\mathbf{-2.3389 \times 10^{-07}}$	$\mathbf{-9.9271 \times 10^{01}}$	Linearly stable
2593.3710	0.148864068660	9.2680×10^{-07}	-9.9271×10^{01}	Linearly unstable
3004.0110	0.138734531175	9.2651	1.2261×10^{02}	Linearly unstable
4003.3912	0.121206091142	3.4088×10^{01}	-1.6445×10^{02}	Linearly unstable
5000	0.109489888792	1.7354×10^{02}	1.1112×10^{02}	Linearly unstable

flow region is linearly stable, while 48.13% is linearly unstable.

Furthermore, the obtained number of secondary vortices in the SS branches for multifarious Dn is figured in a bar diagram in the $(Dn - \theta)$ plane as displayed in Figure 8. It can be apparently seen that the least (2-vortex) and most (7-vortex) number of vortices are produced in the 1st branch only, wherein the 3rd, and 4th branches contain only 4-vortex solutions. Besides, with the increment of Dn, the number of vortices increases as well. Overall, it indicates that the thermo-fluid flow behavior is influenced by heat transfer from the heated walls, buoyancy force, centrifugal force, and pressure effects. These factors collectively lead to the modification and escalation of secondary flows, resulting in an increased number of vortices. Understanding these phenomena is crucial for analyzing and optimizing the performance of the system.

As of Yanase et al.,[36] while heating the sidewalls, the main flow in the duct cross-section turns to secondary flow (this is called flow distortion) resulting in flow asymmetry, as well as the density of the fluid changes near to the walls leads to thermal convection (TC). Therefore, the incorporation of radial flow that is induced by the centrifugal force and the convection due to the temperature difference determines the ensuing flow characteristics in the cross-section. For small pressure gradient number (lower Dn), less CF is seen and TC influences the flow, the resultant secondary accounts for two-vortex solution in the whole cross-section. On the contrary, as Dn increases, correspondingly centrifugal body force rises, instability occurs in the main flow, and re-builds the SF.

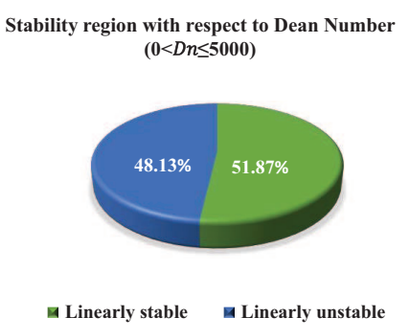

Fig. 7. Linearly stable and unstable region with regard to Dn.

4.1.1. Axial Velocity and Secondary Flow Distribution

The notion of the pattern variation of axial flow (AF) and SF is resulted in the AF distribution and SF distribution diversely. It is stated by Mondal et al.[5] that AF varied throughout the branches of SSs due to the continuous increase of pressure gradient, but the authors did not mention how much velocity can the flow be at a specific grid point. In another research, Ma et al.[37] investigated the flow of electrically conducting fluid (Ag–MgO/water) in a channel with active heaters and coolers in the top and bottom walls. The obtained flow pattern and heat transfer stated that increasing the Reynolds number (Re) changes the velocity distribution. Sarkar and Biswas[38] revealed the velocity distribution for highly established time-periodic flows in cylindrical shape, where the flow is stimulated by the time-periodic behavior of the flow-boundaries. As the default setting of the aspect variable is decreased, it is seen that the velocity profile gets more and more asymmetric. The distribution of axial velocity and secondary flow with respect to grid points is shown in Figures 9 and 10, respectively. The concept is based on the $20 \times 20 = 400$ grid points on the cross-section of the duct, which are gradually directed into the central points, which means the

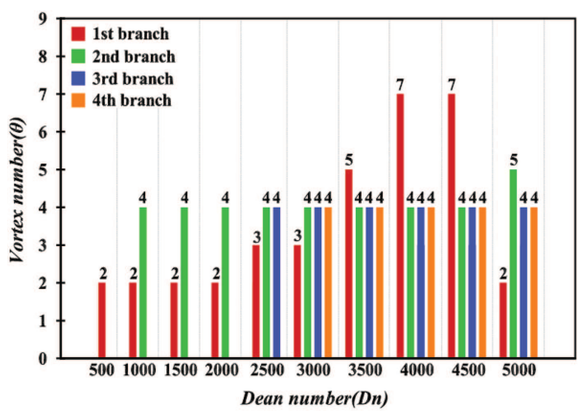

Fig. 8. Number of secondary vortices in the SS branches for $\delta = 0.1$.

grid points are started from the boundary and then ended at the center. Since we have obtained four distinct SSs and different forms of SF, vortex structure, and velocity into the vortex, AV and SF distribution for various *Dn* in the respective steady branches concerning grid points are depicted here.

It is noticed from Figures 9(a)–(d) that velocity on the 1st branch starts with a high-velocity domain near the boundary and then tends to low to the center of the duct due to temperature difference between the walls. With the advancement of *Dn*, the velocity increases on the boundary and the highest velocity is detected at $Dn = 5000$. Apparently, at $Dn = 5000$ in the 2nd branch, mostly negative velocity is created rather than any other branch. This implies that the fluid in this branch is predominantly moving in the opposite direction compared

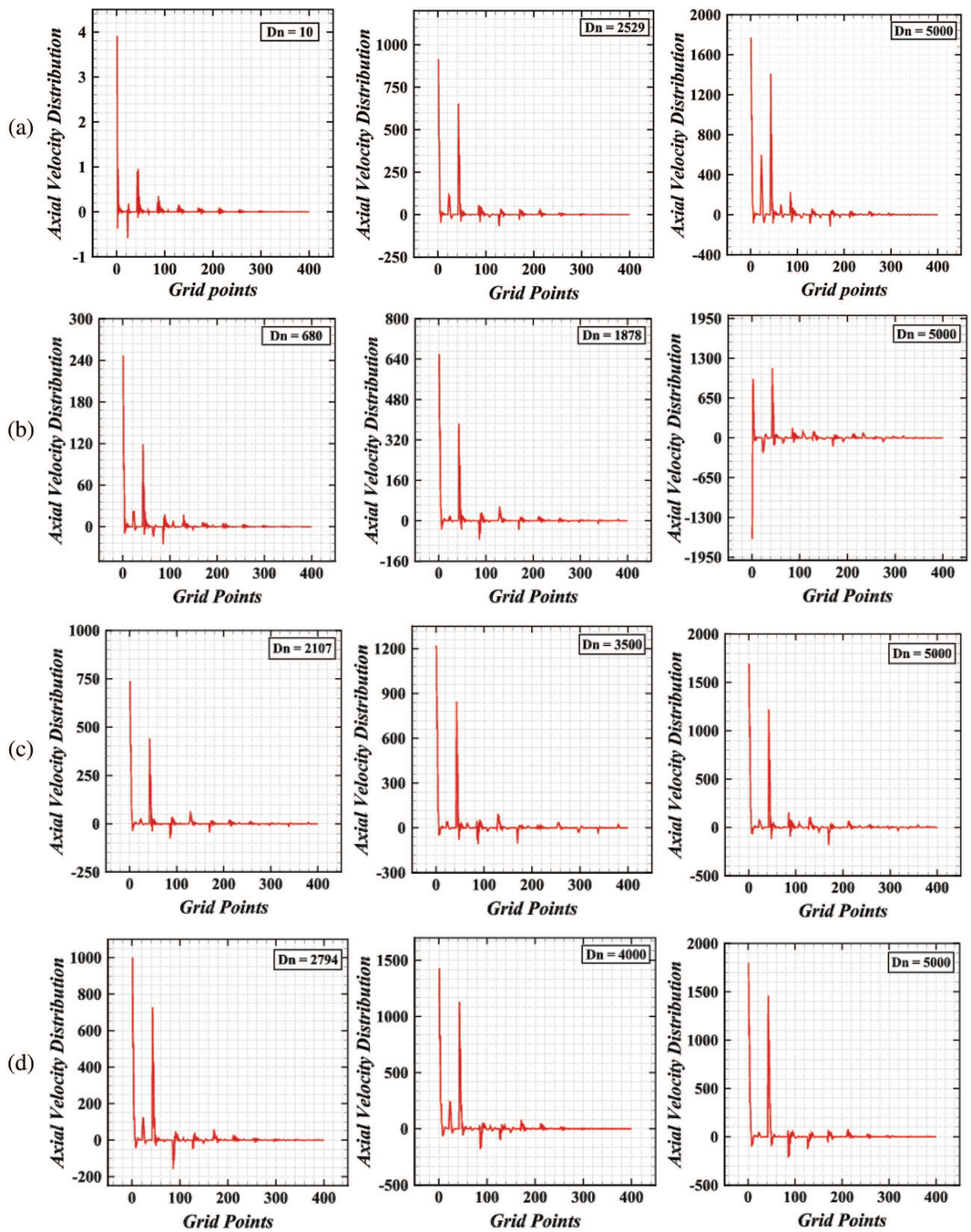

Fig. 9. Axial velocity distribution over the grid points; (a) 1st branch, (b) 2nd branch, (c) 3rd branch, and (d) 4th branch.

ARTICLE

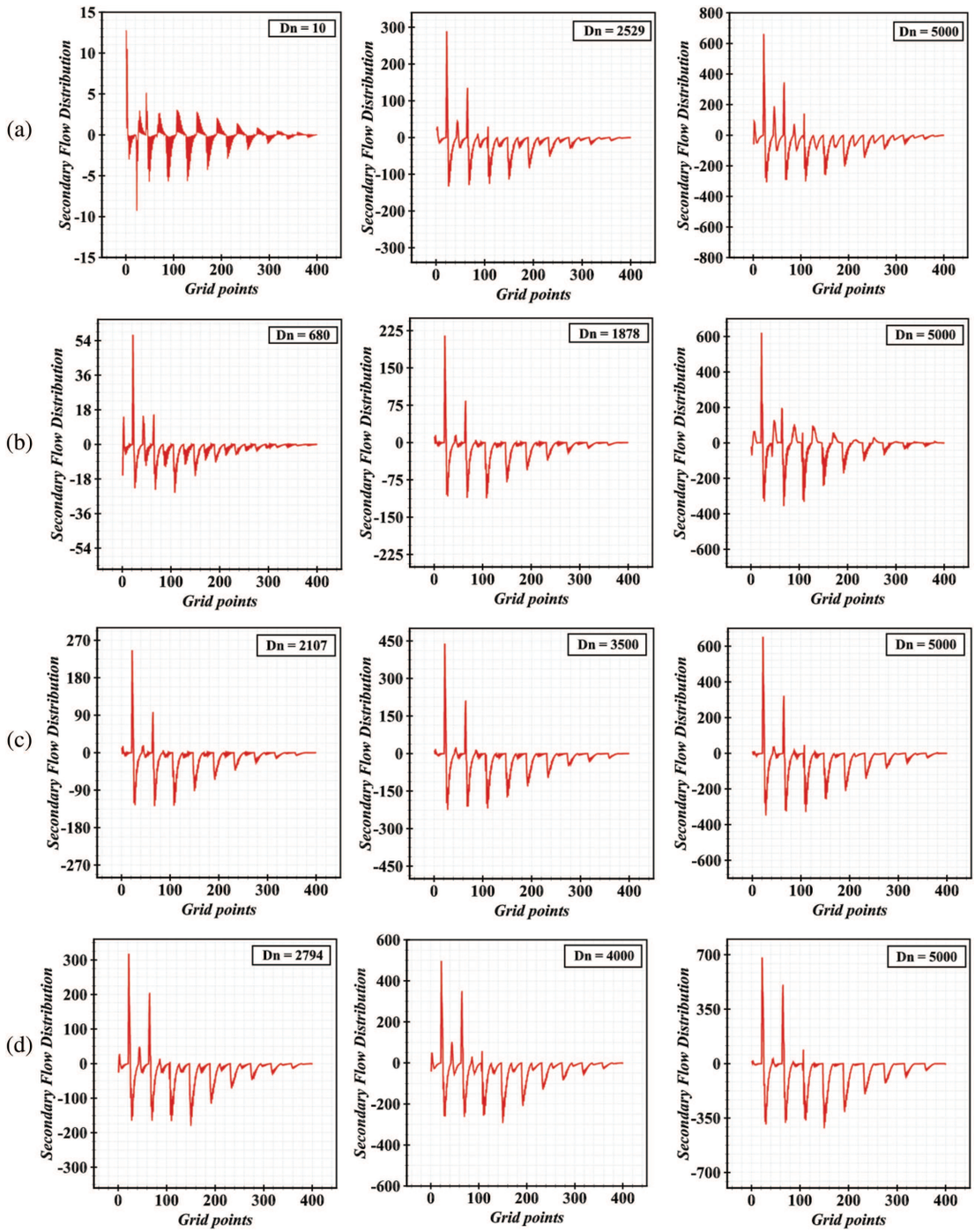

Fig. 10. Secondary flow distribution over the grid points; (a) 1st branch, (b) 2nd branch, (c) 3rd branch, and (d) 4th branch.

to the other branches, possibly due to specific flow conditions or geometrical factors. On the other hand, it is interesting to the study by Dean[10, 11] that a couple of counter-rotating vortices appear on the cross-section of the duct. The upper vortex rotates counter-clockwise while the lower vortex is clockwise in the direction. The swirling motion between these vortices is not identical, suggesting complex fluid dynamics within the flow. It is explained in Figures 10(a)–(d), that for smaller *Dn*, the velocity was too low in both of the vortices. Afterward, the velocity tends to increase with the increase of *Dn* and generated more vortices. Due to the diverse velocity pattern

in the SS branches, they are distinguished by the number of vortices. It is observed from the SF distribution that from the boundary to the center of the duct, it flows like a wave pattern, fluctuating both clockwise and counterclockwise direction. This behavior is likely influenced by the complex interaction between the primary and secondary flows. Dean vortices are created towards the outer concave wall due to centrifugal buoyancy instability. At the same time, these are sometimes generated near the convex wall of the channel due to the reverse flow of the outward secondary flow, as noted by Islam et al.[20] for rotating BRD flow.

4.2. Investigation of Unsteady Flow Transition

The exploration of time-dependent flow using the parametric values in Table II is numerically executed, plotted in the t-λ plane, where necessary phase space is drawn to legitimize the periodicity/multi-periodicity/chaotic behavior.

At first, since we have already found out that up to $Dn = 2593.3709$ in the 1st steady branch, which covers the whole region of Dn in our present study, is linearly stable; so in the UF, it is carefully noticed that the UF behavior is steady-state in this prescribed region and described them in Figure 11. The steady-state flow then switches into the periodic flow after $Dn = 2593.3710$ and remains the same flow up to $Dn = 2909$. In Figure 12(a), the periodic flow for $Dn = 2750$ is illustrated with the same steady lines as used in the bifurcation diagram in Figure 4. The flow vacillates $0.1447 \leq \lambda \leq 0.1455$ above the 2nd branch, lying on the 1st branch. The PS of the reduplicative flow is presented in Figure 12(b) in λ versus γ plane, where $\gamma = \int\int \zeta dxdy$, which confirms the flow periodicity. Thereafter, the flow splits into chaos and consists in the zone, $2910 \leq Dn \leq 3455$. For $Dn = 3000$, the time progression is figured in the t versus λ plane in Figure 13(a). The

flow neither looks periodic nor chaotic; due to this issue, PS is drawn in Figure 13(b), which shows a transitional chaos scheme. Next, in Figures 14(a), a comparatively weak chaotic stream is introduced for $Dn = 3250$, which is ascertained by PS as shown in Figure 14(b). Surprisingly, the chaotic phenomena transmute to multi-periodic flow in

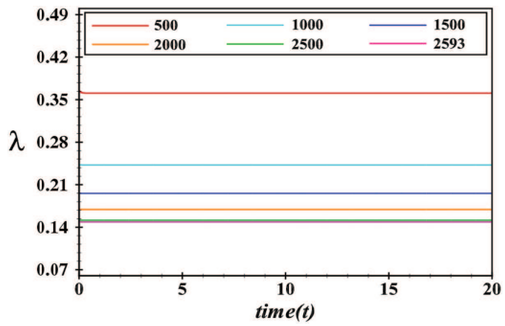

Fig. 11. Time-dependent flow for $500 \leq Dn \leq 2593.371$.

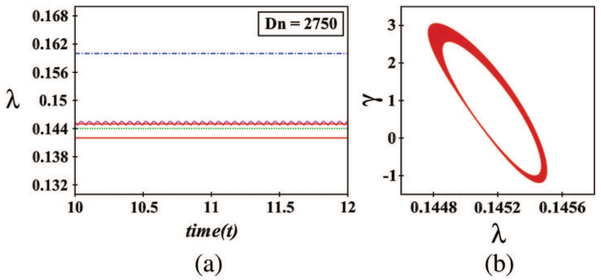

Fig. 12. (a) Time-dependent flow for $Dn = 2750$, (b) phase space.

the territory of Dn, $3456 \leq Dn \leq 3829$. As for verification, for $Dn = 3500$, the multi-periodicity of the flow state is traced out in Figure 15(a) and the PS in Figure 15(b), which vacillates on $0.1333 \leq \lambda \leq 0.1358$ between the 2nd and 4th steady branches. The flow deucedly turns back to a chaotic stream again, starting from $Dn = 3830$ and continues with the increment of Dn no matter where it is stopped. For instance, for $Dn = 5000$, the chaotic stream is portrayed in Figure 16(a), and the associated PS is presented in Figure 16(b). The irregularities of the flow have a maximum resistance coefficient at $\lambda = 0.1448$ and minimum at $\lambda = 0.1095$. In brief, the transition from linearly stable steady-state flow to periodic flow and eventually to chaos occurs as the parameter Dn is varied. Phase space analysis provides a valuable tool to visualize the periodicity of the flow and confirm the transition between different flow regimes. Chaos arises due to the nonlinear interactions between different components of the flow system. Even small changes in initial conditions or system parameters can lead to drastically different flow patterns, making it challenging to predict the long-term behavior of the system.

4.2.1. Proportion of Unsteady Flow and Vortex Variation

In Section 4.2, we have already discussed the region of individual flow state, i.e., the obtained region of steady-state flow is for $0 < Dn \leq 2593.3709$, periodic for $2593.3710 \leq Dn \leq 2909$, multi-periodic $3456 \leq Dn \leq 3829$, and the chaotic for $2910 \leq Dn \leq 3455$ and $3830 \leq Dn \leq 5000$. In this sub-section, we briefly show the percentage of individual flow states in a pie chart in Figure 17.

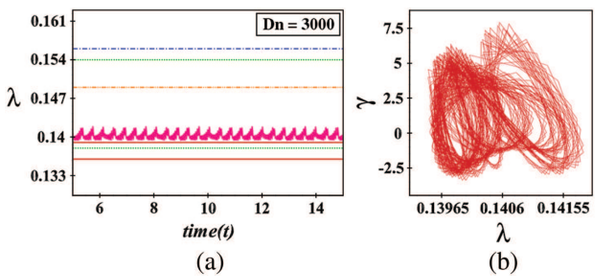

Fig. 13. (a) Time-dependent flow for $Dn = 3000$, (b) phase space.

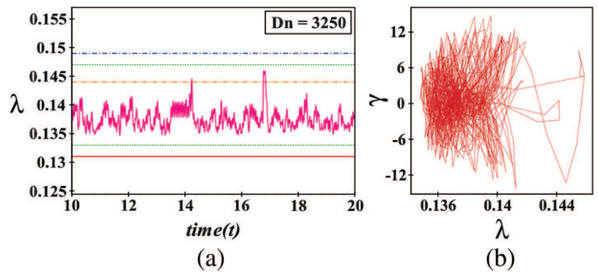

Fig. 14. (a) Time-dependent flow for $Dn = 3250$, (b) Phase space.

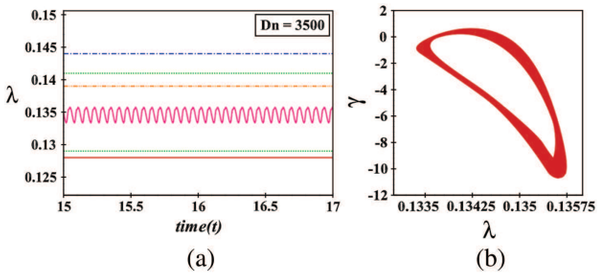

Fig. 15. (a) Time-dependent flow for $Dn = 3500$, (b) phase space.

It is seen that the steady-state flow occupies the maximum region of *Dn*, almost 51.87%; afterward, combining two distinct regions of *Dn,* chaotic flow covers 34.54%, and periodic flow exists about 13.78%. Besides, the composition of secondary vortices in the UF is computed for multitudinous *Dn* in the $(\theta - Dn)$ plane, as presented in Figure 18. We have noticed that the number of vortices is increased with the emergence of *Dn,* and a maximum of two- to a five-vortex solution is revealed in the chaotic stream. This study shows that chaotic flow has the maximum number of secondary vortices compared to other cases. As *Dn* increases, the fluid particles move in closer to the wall and create friction with one another; at some point, Dean vortices from outside the channel wall become crucial in transmitting heat from the external wall to the fluid.

4.3. Diversification of the Nusselt Number (*Nu*)

The Nusselt number (*Nu*) is enumerated as an intimation of CHT from the wedges to the fluid to speculate

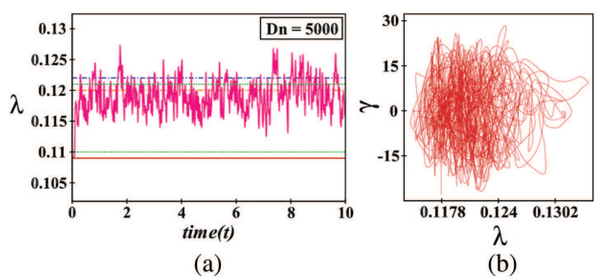

Fig. 16. (a) Time-dependent flow for $Dn = 5000$, (b) phase space.

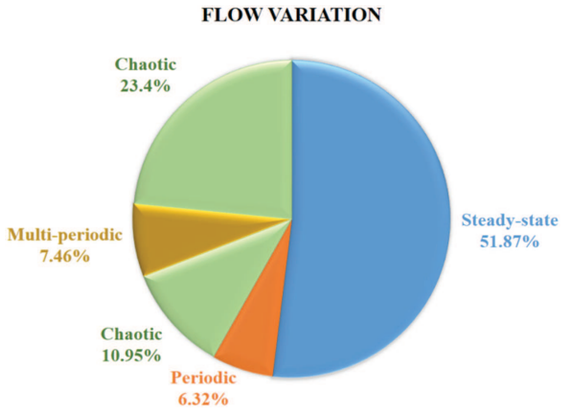

Fig. 17. Unsteady flow percentage over *Dn*.

the energy distribution through Eqs. (16) and (17). Since both steady and unsteady flow have been discussed in this study, *Nu* has been calculated for both types of solutions. Since the first steady branch is the only one that has fully conquered the region of *Dn*, Eq. (16) is used to compute the *Nu* of SS, while Eq. (17) is used to get the *Nu* of UF. Selimefendigil et al.[39] showed the variation in *Nu* with *Re* for various inclination angle of the channel and assumed to be increased in *Nu* for higher inclination angle in lower branching channel. Based on the shape of cavities (square and circular), thermal management was analysed by Saha et al.[40] The study showed the efficiency of geometrical shape of the body using *Nu* variation for various Rayleigh number and inclination angle. In this study, a distinct approach is applied to enumerate the *Nu* from the unsteady solutions, e.g., for a particular *Dn*, first of all, time evolution is performed, and then from the entire evolution, the average of *Nu* is determined. The diversity of *Nu* is shown in Figure 19 on the *Dn-Nu* plane, where the blue and red solid lines represent the *Nu* for SS and the symbolically delineated circle and triangle, the time average of *Nu* for unsteady solutions for both cooling and heating walls respectively. It is observed that the enhancement rate of *Nu* on the heated walls is greater than the cooled walls. For high-pressure gradients, the fluid is mixed up

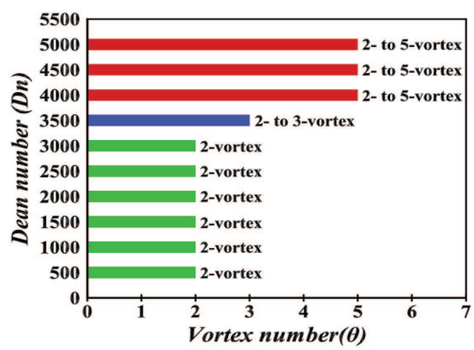

Fig. 18. The number of secondary vortices in the unsteady flow for $\delta = 0.1$.

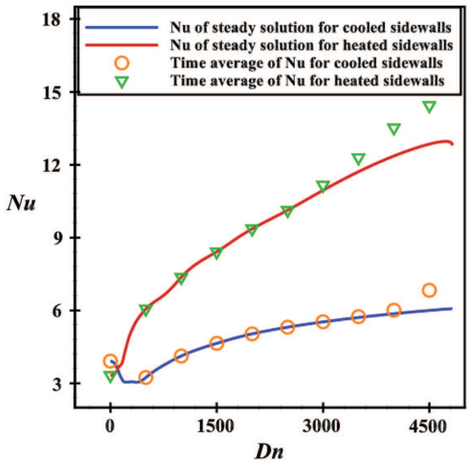

Fig. 19. Diversity of *Nu* for multifarious *Dn* in the *Dn-Nu* plane.

and produces more vortices which affect the enhancement of the heat transfer, visible in Figure 19.

5. DISCUSSIONS

Fluid flow and HT in a curved channel is frequently used in numerous industrial applications including solar panels, metallic industry, polymer industry and air conditioning equipment. Before conducting their research, engineers must prioritize maximizing equipment expenses as well as bending channel (BC) usage comfort. A bending channel is the appropriate way for researchers to maximize costs and convenience for applications in mechanical and chemical engineering; for instance, using the BC to create an air conditioner is the most effective method in terms of air conveyance. Therefore, keeping these issues in mind, this paper presents some substantial results on fluid flow and thermal enhancement in a bending square-shaped channel.

Nowruzi et al.[41] used energy gradient method to depict the hydrodynamic unsteadiness in the BC for different aspect ratio (AR) where aspects of unsteady behavior with the grid-sizes impact on fluid transition were missing. Hasan et al.[35] carried out a spectral-based numerical approach to demonstrate the relationship among bifurcation structure, linear stability and flow transitions for a bending square channel (BSC) flow. Li et al.[42] examined SF deviation for different curvatures by using 3-D contours and explored point-by-point variation in Dean flow for varying *Ar* however their investigation of HT impacts on the Dean flow was limited. Chamkha et al.[43,44] and Kumar et al.[45] visualized the velocity profiles by the presence of buoyancy effects in a isothermal–isothermal wall heating conditions for a vertical channel. In an upward flow, as the Gr/Re number increases, the momentum of the flow near the hot right wall increases, resulting in an asymmetric velocity profile. Recently, Yadegari et al.[46] conducted a through analysis of the CF, turning angle and curvature ratio of the curved diffusers with CRD; however, their work was limited in that it did not adequately describe transient behavior with vortex structure. Although Mondal et al.[47] previously demonstrated this transitional behavior for two distinct *Dn* parameters for varied *Ar* but the consequences of periodic, multi-periodic, and even chaotic behavior with vortex structure on transient flow were absent in their study. The current analysis, however, fills this gap. Recently, Islam et al.,[48] Dolan et al.[49] and Mondal et al.[50] used a rotating CRD heating from the outer wall and cooling from the inner wall and inspected the effects of Coriolis force on the flow pattern. The working fluid was controlled by a non-dimensional parameter called the Taylor number (*Tr*). Stability analysis of the steady solutions were absent in their study. Though they focused on showing the vortex structure of the flow for both steady and unsteady solutions, there was no information about the grid-point-wise axial and secondary flow distribution. The present study attempts to fulfill this shortcoming very meticulously. Very recently, Adhikari et al.[26] explored the pressure-induced flow instability for a loosely BC with curvature 0.001. The authors[26] failed to explain the relative position of the solution branches and no stability analysis was performed in their study; this issue is resolved in the present study. The present study deals with the thermal boundary conditions for the square-shaped geometrical channel with curvature 0.1 having temperature variations among the walls. Convective heat transfer by showing the variation of the Nusselt number with respect to *Dn*, rather than the temperature gradient, is accomplished in this study which is very convenient for the researchers to get a clear idea about HT in the flow. Additionally, in the present study that provides a strong understanding of a BC through flow state oscillations, hydrodynamic unsteadiness and the creation of longitudinal vortex structure have been examined. For convenience, the summary of vortex structure of secondary flows are also shown in a bar diagram. The ongoing investigation provides detailed explanations of overall HT and fluid mixing in a CSC.

6. CONCLUDING REMARKS

The present study speculated two-dimensional viscous incompressible fluid flow driven by the pressure gradient ($0 < Dn \leq 5000$) and numerically executed by spectral scheme using a bent square channel with curvature 0.1. The study develops a computational framework for the non-isothermal flow where solution structure, linear stability and transient behavior of the flow have been discussed in detail. Effects of pressure gradient on fluid flow and energy distribution with vortex structure of secondary flows are discussed explicitly. Some key findings of this study are:

- Four distinct branches of steady solutions are observed; among those branches, only the 1st branch is

linearly stable in a particular region ($0 < Dn \leq 2593.3709$) while the other branches contain no stable regions.

- The first branch is formed with two-, three- and five- to seven-vortex solutions. The 2nd branch is built in two- to five-vortex solutions, and the 3rd and 4th branches consist of four-vortex solutions only.
- The altercation of flow-state is unerringly inspected, i.e., the obtained region of steady-state flow is $0 < Dn \leq 2593.3709$, periodic for $2593.3710 \leq Dn \leq 2909$, multi-periodic in the region of $3456 \leq Dn \leq 3829$, and the chaotic for $2910 \leq Dn \leq 3455$ and $3830 \leq Dn \leq 5000$.
- The steady-state flow is almost 51.87%; afterward, combining two distinct regions of *Dn,* chaotic flow covers 34.54%, and periodic flow exists about 13.78% of the total flow region.
- In the unsteady flow manner, the number of secondary vortices increases with the emergence of *Dn,* and a maximum of two- to a five-vortex solution is revealed in the chaotic stream.
- The diversification of *Nu* is analyzed, and it is revealed that the enhancement rate of *Nu* on the heated walls is greater than the cooling walls. The calculated Nusselt number results reveal that for *Dn* values greater than zero, the Nusselt number initially exhibited higher values on the cold walls than on the heated sidewalls. However, at $Dn = 102.67$, the Nusselt number became equal on both sides, after which it started increasing rapidly on the heated sidewalls.
- For high-pressure gradients ($Dn \geq 3500$), the fluid is mixed up and produces more vortices, which substantially affects the enhancement of heat transfer in the fluid.

The findings of this study would improve the knowledge of the transitional flow behavior and corresponding energy distribution for a bending channel. The future study will analyze the heat transfer for different configurations.

NOMENCLATURE

Dn	Dean number
Gr	Grashof number
Pr	Prandtl number
A_r	Aspect ratio
δ	Curvature
ν	Kinetic viscosity
g	Gravitational acceleration
B	Momentum factor
κ	thermal conductivity
$\Im$	Temperature
∇	Gradient operator
u, v, w	Velocity components
ζ	Stream function
P	Pressure
U_0	Centre velocity
T	Time
Ω_n	Chebyshev polynomials
λ	Resistance coefficient
d_h	Hydraulic diameter
$\langle\tilde{\alpha}\rangle$	Mean axial velocity
ρ	Fluid density
Nu	Nusselt number
HT	Heat transfer
FF	Fluid flow
CS	Cross-section
BP	Bent pipe
CF	Centrifugal force
CD	Curved duct
BS	Bifurcation structure
BD	Bent duct
SF	Secondary flow
CRD	Curved rectangular duct
AF	Axial flow
UF	Unsteady flow
SS	Steady solution
PS	Phase space
PSD	Power spectrum density
CHT	Convective heat transfer
HC	Convection of heat
BSD	Bent square duct
CSD	Curved square duct
AV	Axial velocity

Declaration

All authors equally contributed to the study conception and design, material preparation, data collection and analysis. All authors read and approved the final manuscript.

Data Availability

Data will be available upon reasonable request.

Conflicts of Interest

No conflicts of interest are associated with this study.

Acknowledgment: The authors acknowledge the computational facility at Jagannath University.

References and Notes

1. R. N. Mondal, M. Z. Islam, and M. S. Islam, *Procedia Engineering* 56, 179 **(2013)**.
2. R. N. Mondal, M. Z. Islam, and R. Perven, *Procedia Engineering* 90, 261 **(2014)**.
3. A. Goharzadeh and P. Rodgers, *Fluids* 6, 184 **(2021)**.
4. P. Hille, R. Vehrenkamp, and E. O. Schulz-Dubois, *J. Fluid Mech.* 151, 219 **(1985)**.
5. R. N. Mondal, M. S. Uddin, and S. Yanase, *Int. J. Fluid Mech. Research* 37, 85 **(2010)**.
6. D. Chatterjee, N. Biswas, N. K. Manna, and S. Sarkar, *International Journal of Mechanical Sciences* 238, 107852 **(2023)**.
7. Y. Q. Song, N. Izadpanahi, M. A. Fazilati, Y. P. Lv, and D. Toghraie, *International Communications in Heat and Mass Transfer* 125, 105328 **(2021)**.
8. S. Parvin, R. Nasrin, M. A. Alim, N. F. Hossain, and A. J. Chamkha, *Int. J. Heat Mass Transfer* 55, 5268 **(2012)**.

9. D. Toghraie, R. Mashayekhi, H. Arasteh, S. Sheykhi, M. Niknejadi, and A. J. Chamkha, *International Journal of Numerical Methods for Heat & Fluid Flow* 30, 1795 (**2019**).
10. W. R. Dean, *Phill. Mag*. 4, 280 (**1927**).
11. W. R. Dean, *Proceedings of the Royal Society of London. Series A, Containing Papers of a Mathematical and Physical Character* 121, 402 (**1928**).
12. R. N. Mondal, Y. Kaga, and T. Hyakutake, and S. Yanase, *Trans. ASME. J. Fluids Eng.* 128, 1013 (**2006**).
13. M. S. Hasan, R. N. Mondal, and S. Yanase, *AIP Conference Proceedings* 2324, 050020 (**2021**).
14. M. S. Hasan, R. N. Mondal, and G. Lorenzini, *Chinese Journal of Physics* 77, 1305 (**2022**).
15. M. S. Hasan, M. T. Mollah, D. Kumar, R. N. Mondal, and G. Lorenzini, *International Journal of Applied Mechanics and Engineering* 26, 29 (**2021**).
16. S. Yanase and K. Nishiyama, *Journal of Physical Society of Japan* 57, 3790 (**1988**).
17. R. N. Mondal, M. Z. Islam, M. M. Islam, and S. Yanase, *Thammasat Int. J. Sci. Tech*. 20, 1 (**2015**).
18. A. J. Chamkha, *Int. J. Heat Fluid Flow* 21, 740 (**2000**).
19. S. C. Ray, M. S. Hasan, and R. N. Mondal, *Mathematical Modelling of Engineering Problems* 7, 31 (**2020**).
20. M. Z. Islam, R. N. Mondal, and M. M. Rashidi, *Computers and Fluids* 149, 41 (**2017**).
21. R. K. Chanda, M. K. Uddin, and R. N. Mondal, *Int. J. Adv. Appl. Math. and Mech.* 8, 48 (**2021**).
22. R. K. Chanda, M. S. Hasan, M. M. Alam, and R. N. Mondal, *Mathematical Modelling of Engineering Problems* 7, 501 (**2020**).
23. R. K. Chanda, M. S. Hasan, M. M. Alam, and R. N. Mondal, *Int. J. Appl. Comput. Math.* 7, 146 (**2021**).
24. R. K. Chanda, M. S. Hasan, G. Lorenzini, and R. N. Mondal, *Journal of Engineering Thermophysics* 30, 243 (**2021**).
25. N. K. Manna, N. Biswas, D. K. Mandal, U. K. Sarkar, H. F. Öztop, and N. Abu-Hamdeh, *International Journal of Numerical Methods for Heat & Fluid Flow* 33, 1249 (**2023**).
26. S. C. Adhikari, R. K. Chanda, S. Bhowmick, R. N. Mondal, and S. C. Saha, *Energy Engineering* 119, 429 (**2021**).
27. M. S. Hasan, R. N. Mondal, and G. Lorenzini, *Chinese Journal of Physics* 67, 428 (**2020**).
28. K. H. Winters, *J. Fluid Mech*. 180, 343 (**1987**).
29. R. N. Mondal, Y. Kaga, T. Hyakutake, and S. Yanase, *Fluid Dynamics Research* 39, 413 (**2007**).
30. D. Gottlieb and S. A. Orszag, Numerical Analysis of Spectral Methods: Theory and Applications. Society for Industrial and Applied Mathematics (**1977**).
31. M. S. Hasan, R. N. Mondal, and G. Lorenzini, *Chinese Journal of Physics* 77, 189 (**2022**).
32. M. S. Hasan, S. N. Dolon, H. S. Chakraborty, R. N. Mondal, and G. Lorenzini, *Journal of Applied and Computational Mechanics* 7, 1435 (**2021**).
33. L. Wang, O. Pang, and L. Cheng, *Chaos. Solitons and Fractals* 26, 337 (**2005**).
34. L. Wang and T. Yang, *Physica D: Nonlinear Phenomena* 200, 296 (**2005**).
35. M. S. Hasan, S. Rashid, S. N. Dolon, R. K. Chanda, M. M. Islam, R. N. Mondal, and G. Lorenzini, *Reports in Mechanical Engineering* 2, 86 (**2021**).
36. S. Yanase, *Eur. J. Mech. B Fluids* 10, 321 (**1991**).
37. Y. Ma, R. Mohebbi, M. M. Rashidi, and Z. Yang, *Int. J. Heat Mass Transfer* 137, 714 (**2019**).
38. U. K. Sarkar and N. Biswas, *SN Appl. Sci.* 3, 339 (**2021**).
39. F. Selimefendigil, H. F. Öztop, and A. J. Chamkha, *International Journal of Numerical Methods for Heat & Fluid Flow* 30, 1755 (**2020**).
40. A. Saha, N. K. Manna, K. Ghosh, and N. Biswas, *The European Physical Journal Special Topics* 231, 2509 (**2022**).
41. H. Nowruzi, H. Ghassemi, and S. S. Nourazar, *Engineering Science and Technology, An International Journal* 23, 334 (**2020**).
42. Y. Li, X. Wang, B. Zhou, S. Yuan, and S. K. Tan, *Int. J. Heat Fluid Flow* 68, 189 (**2017**).
43. A. J. Chamkha, *Int. J. Heat Mass Transfer* 45, 2509 (**2002**).
44. A. J. Chamkha, T. Groşan, and I. Pop, *International Communications in Heat and Mass Transfer* 29, 1119 (**2002**).
45. J. P. Kumar, J. C. Umavathi, A. J. Chamkha, and I. Pop, *Applied Mathematical Modelling* 34, 1175 (**2010**).
46. M. Yadegari and A. B. Khoshnevis, *Eur. Phys. J. Plus* 135, 548 (**2020**).
47. R. N. Mondal, T. Watanabe, M. A. Hossain, and S. Yanase, *J. Thermophys Heat Transfer* 31, 243 (**2017**).
48. M. Z. Islam, R. N. Mondal, and S. C. Saha, *Energy Engineering* 119, 453 (**2022**).
49. S. N. Dolon, M. S. Hasan, G. Lorenzini, and R. N. Mondal, *The European Physical Journal Plus* 136, 1 (**2021**).
50. R. N. Mondal, M. S. Hasan, M. S. Islam, M. Z. Islam, and S. C. Saha, *Int. J. of Heat and Technology* 39, 1213 (**2021**).

ARTICLE